Research Square

Preprints are preliminary reports that have not undergone peer review.
They should not be considered conclusive, used to inform clinical practice,
or referenced by the media as validated information.

Co-exposure to ionizing irradiation and high-fat diet induces low-grade neuroinflammation and neurovascular remodeling in the mouse hippocampus

Léa Ould Boukhitine
Autorité de Sûreté Nucléaire et de Radioprotection, PSE-SANTE/SESANE/LRTOX
Chloé Brizais
Autorité de Sûreté Nucléaire et de Radioprotection, PSE-SANTE/SESANE/LRTOX
Florence Bachelot
Autorité de Sûreté Nucléaire et de Radioprotection, PSE-SANTE/SESANE/LRTOX
Yasmine Ebid
Autorité de Sûreté Nucléaire et de Radioprotection, PSE-SANTE/SESANE/LRTOX
Imane Lahyouli
Autorité de Sûreté Nucléaire et de Radioprotection, PSE-SANTE/SESANE/LRTOX
Chrystelle Ibanez
Autorité de Sûreté Nucléaire et de Radioprotection, PSE-SANTE/SESANE/LRTOX
Imène Garali
Autorité de Sûreté Nucléaire et de Radioprotection, PSE-SANTE/SESANE/LRTOX
Stéphane Grison
Autorité de Sûreté Nucléaire et de Radioprotection, PSE-SANTE/SESANE/LRTOX
Mouna Chajadine
Autorité de Sûreté Nucléaire et de Radioprotection, PSE-SANTE/SESANE/LRTOX
Justyne Feat-vetel
Autorité de Sûreté Nucléaire et de Radioprotection, PSE-SANTE/SESANE/LRTOX
Celine Gloaguen
Autorité de Sûreté Nucléaire et de Radioprotection, PSE-SANTE/SESANE/LRTOX
Christelle Durand
Autorité de Sûreté Nucléaire et de Radioprotection, PSE-SANTE/SESANE/LRTOX
Dmitry Klokov
Autorité de Sûreté Nucléaire et de Radioprotection, PSE-SANTE/SESANE/LRTOX
Boris Manoury
Université Paris-Saclay, Inserm, UMR-S 1180

Teni G. Ebrahimian

teni.ebrahimian@asnr.fr

Autorité de Sûreté Nucléaire et de Radioprotection, PSE-SANTE/SESANE/LRTOX

Article

Keywords: co-exposure, gamma-radiation, high-fat diet, hippocampus, microcirculation

Posted Date: November 3rd, 2026

DOI: https://doi.org/10.21203/rs.3.rs-11190223/v1

License: This work is licensed under a Creative Commons Attribution 4.0 International License.
Read Full License

Additional Declarations: No competing interests reported.

Abstract

Epidemiological evidence suggests that exposure to ionizing radiation (IR) may increase the risk of cerebrovascular diseases, yet the long-term effects of moderate doses and their interaction with obesity-related metabolic stress remain unclear. This study investigated whether high-fat diet (HFD) modifies cerebrovascular responses to moderate doses of gamma radiation. Male C57BL/6J mice were exposed to acute whole-body gamma radiation at 300 or 1000 mGy and maintained six months on either a standard diet (SD) or a HFD. Hippocampal oxidative stress, inflammation, endothelial activation, and vascular remodeling markers were assessed by RT-qPCR, immunofluorescence, and Western blot. Untargeted plasma metabolomics was performed to identify systemic metabolic alterations associated with irradiation.

Exposure to 300 mGy did not significantly alter hippocampal vascular features, either alone or with HFD. In contrast, co-exposure to 1000 mGy and HFD induced low-grade neuroinflammation, characterized by increased microglial activation, upregulation of chemokine expression, and increased LYVE-1 immunostaining, suggesting recruitment of perivascular macrophages. Co-exposure also resulted in increased hippocampal vascular density and elevated ZO-1 expression, suggesting vascular remodeling. Metabolomic pathway enrichment analysis identified purine metabolism and the malate-aspartate shuttle as major pathways associated with irradiation-induced metabolic changes. These findings demonstrate that metabolic stress enhances the long-term neurovascular consequences of moderate-dose gamma radiation.

Introduction

Eexposure to ionizing radiation (IR) is a major public health concern due to its potential long-term effects on multiple organ systems, including the cardiovascular system. Both epidemiological [1, 2] and experimental studies [3, 4] revealed that exposure to high doses of ionizing radiation is associated with an increased risk of cardiovascular disease.

Cardiovascular disease has been recognized as a relevant late effect of ionizing radiation exposure. Reflecting this concern, the International Commission on Radiological Protection (ICRP) has considered circulatory diseases in its recommendations and identified a threshold dose of 0.5 Gy for radiological protection purposes [5]. Beyond radiological protection considerations, increasing epidemiological and experimental evidence suggests that radiation exposure can adversely affect cardiovascular health through mechanisms involving endothelial dysfunction, inflammation, and tissue remodeling [6, 7]. However, the biological responses of cardiovascular tissues to low and moderate radiation doses remain incompletely characterized, warranting further investigation.

Circulatory diseases are multifactorial, many risk factors influence their development and severity, including modifiable factors such as lifestyle habits. These lifestyle factors may expose individuals to multiple biological stressors, including consumption of a high-fat diet (HFD) and the resulting metabolic disturbances associated with obesity.

Experimental rodent models of diet-induced obesity demonstrate impairment of the neurovascular unit and endothelial dysfunction, characterized by oxidative stress, inflammation, and increased in blood-brain barrier permeability [5]. The hippocampus is especially vulnerable to HFD-induced disruption of the blood-brain barrier [6].

The cerebral microvasculature is particularly sensitive to both metabolic and inflammatory insults. Alterations of the neurovascular unit may compromise cerebral blood flow regulation, blood-brain barrier integrity, and neuronal function, potentially contributing to cognitive decline and neurovascular disease. However, despite growing evidence that both moderate-dose radiation and obesity independently affect vascular homeostasis, little is known about how metabolic stress influences the long-term cerebrovascular response to moderate-dose radiation, particularly the neurovascular unit. Some studies focused on the effects of repeated irradiation and found that co-exposure with a HFD amplifies vascular injury by lipid deposition in damaged arterial walls, enhanced inflammation, and activation of oxidative stress pathways [7–9]. Furthermore, studies on the impact of moderate-dose radiation on metabolism in animals co-stressed by a high-fat diet, are sparce. A recent study supports the hypothesis that low-dose radiation promotes alterations in the metabolomic profile, thereby exacerbating HFD-induced obesity [10].

The present study aimed to investigate the effects of acute external exposure to moderate doses of gamma radiation on cerebral microcirculation in mice, in the presence or absence of a HFD, a major cardiovascular risk factor. We hypothesized that irradiation would disrupt neurovascular homeostasis through oxidative stress, inflammatory responses, endothelial dysfunction, and metabolic alterations, and that these effects could be modified or exacerbated by HFD-induced metabolic dysfunction. To address this hypothesis, we assessed vascular, molecular, and metabolomic changes following irradiation alone or in combination with HFD.

Results

After 6 months, HFD-fed mice exhibited a significant increase in body weight compared with SD-fed mice, while irradiation did not significantly affect body-weight gain. Body weight evolution curves are presented in supplementary Figure S1.

No difference in oxidative stress parameters 6 months after co-exposure

NADPH oxidase activation induces production of reactive oxygen species (ROS), especially superoxide anion O2-. We measured gene expression of NADPH oxidase subunits by RT-qPCR and found no differences in expression following exposure to irradiation and/or a high-fat diet (Fig. 1A).

We observed no significant differences in DHE staining intensity in hippocampus sections across the experimental groups, indicating no difference in the level of superoxide anion $O_2^{\cdot -}$ production. (Fig. 1B

and 1C) Then, we looked at the expression of the *Sod1*, *Sod2* (encoding superoxide dismutase 1 and 2), and *Cat1* (catalase), as they are involved in regulating the redox balance. No significant change was observed in any group for any of these antioxidant genes (Fig. 1D). Taken together, these findings suggest that neither irradiation nor HFD, alone or in combination, induced sustained oxidative stress in the hippocampus 6 months after exposure.

Microglial activation in the hippocampus and over-expression of inflammatory genes after co-exposure to 1000 mGy and a high-fat diet

Next, we examined key inflammatory response indicators in the hippocampus, focusing on microglial cells, the resident macrophages of the central nervous system that play a key role in neuroinflammation following exposure to various stressors. Microglial responses were assessed by immunostaining for the microglial marker Iba1. We analyzed both microglial cell density and activation phenotype in hippocampus sections collected 6 months following irradiation.

First, microglial density did not differ significantly across the experimental groups (Fig. 2A), suggesting that irradiation and/or HFD did not induce microglial proliferation, migration, or infiltration. Because microglia may participate in a neuroinflammatory response by adopting a wide range of activation states, spanning from pro-inflammatory (M1-like) to anti-inflammatory (M2-like) phenotypes, microglial activation was scored.

Our activation score was based on morphological profil and ranged from 0 to 3. We did not detect any hippocampus slides with a general microglial activation score of 2 or 3. However, we observed microglia with an activation score of 1, characterized by shortened processes and a larger cell body (Fig. 2B). In mice exposed to 1000 mGy and HFD, we observed a significant increase in microglia displaying an early activation stage phenotype compared to the control group, non-irradiated fed with a standard diet (Fig. 2C) (chi-square test, $p = 0.02$).

To further characterize the nature of this microglial activation, we next assessed the expression of genes associated with pro- and anti-inflammatory pathways in the hippocampus.

We assessed the mRNA expression of *Nfkb1* (p50) and *Nfkb2* (p100), two transcription factors involved in microglial activation and central regulators of inflammatory signaling. We observed a significant upregulation of both *Nfkb1* and *Nfkb2* in mice co-exposed to 1000 mGy irradiation and HFD, compared to the control group sham-irradiated fed SD (Fig. 2D, $p < 0.001$ for both). By contrast, mice exposed to 300 mGy while maintained on a standard diet exhibited downregulation of *Nfkb1* and *Nfkb2* expression (both $p = 0.003$), suggesting a reduced activation of inflammation.

In addition, a significant increase in the expression of chemokine genes *Ccl2*, *Ccl3*, and *Ccl5* (respectively $p = 0.001$; $p < 0.001$; $p = 0.005$) were observed in the group co-exposed to 1000 mGy and HFD compared to the control group sham-irradiated fed SD (Fig. 2E). These chemokines are known to contribute to immune cell recruitment and neuroinflammatory responses.

However, the cytokine expression profile revealed a more nuanced inflammatory response. While increased microglial activation score and expression of *Nfkb* and chemokines genes are consistent with activation of inflammatory pathways, *Il6* expression was significantly decreased following exposure to 1000 mGy alone ($p = 0.03$) and in combination with HFD ($p < 0.001$). Conversely, expression of *Il11*, a cytokine generally associated with anti-inflammatory and tissue protective responses, was increased in the 1000 mGy ($p = 0.040$) and 1000 mGy + HFD ($p = 0.025$) groups compared to the control group sham-irradiated fed SD (Fig. 2F). Taken together, these findings suggest that exposure to 1000 mGy induces an enhanced chemokine signaling rather than a classical pro-inflammatory cytokine response. This is potentiated by the metabolic stress, translating into partial microglial activation in the 1000 mGy + HFD group.

To further investigate whether this chemokine-rich environment was associated with the recruitment of perivascular immune cells, we evaluated perivascular macrophages by Lyve-1 immunostaining. A significant increase in Lyve-1 staining intensity was observed exclusively in mice co-exposed to 1000 mGy and HFD (Fig. 2G and 2H, p = 0.009) compared to the control group, suggesting an increased abundance of perivascular macrophages in this group. This observation is consistent with the elevated chemokine expression detected in the hippocampus and supports the presence of a localized neuroimmune response following combined irradiation and metabolic stress

No signs of endothelial dysfunction despite evidence of endothelial inflammatory activation

To determine whether the inflammatory profile observed in the hippocampus is associated with endothelial dysfunction, we examined the expression of endothelial adhesion molecules (Fig. 3A). No significant differences were detected in the expression of *Pecam1* and *Vcam1* among the experimental groups. However, *Icam1* expression was significantly increased in mice co-exposed to 1000 mGy irradiation and a HFD ($p = 0.044$), consistent with the inflammatory phenotype observed in this group.We next investigated endothelial nitric oxide synthase (*eNOS*), a key enzyme responsible for nitric oxide production and an essential regulator of endothelial function and vascular homeostasis. Analysis of both *eNOS* mRNA (Fig. 3B), total protein expression, and level of phosphorylation at the activating serine 1177 revealed no significant differences across experimental groups (Fig. 3C and 3D). Although no evidence of overt endothelial dysfunction was detected, vascular inflammation may contribute to structural vascular alterations, including remodeling and angiogenesis. We therefore next investigated markers of vascular remodeling and angiogenic responses.

Increase in vascular density and signs of early remodeling following co-exposure to 1000 mGy and a high-fat diet

Double immunofluorescence staining with CD31 and α-SMA revealed a significant increase in the surface area occupied by non-muscular vessels (represented by vessel CD31-positive and α-SMA-

negative) within the hippocampus of mice co-exposed to 1000 mGy irradiation and HFD, compared to the control group sham-irradiated fed SD ($p = 0.016$) (Fig. 4A and 4B).

Capillaries are covered by pericytes, contractile cells that contribute to vessel stabilization and maintenance of blood-brain integrity. To evaluate pericyte coverage, we quantified the ratio of the PDGFR-β-positive pericyte area to the CD31-positive vascular area. Immunofluorescence co-staining with CD31 and PDGFR-β showed no significant difference in pericyte coverage across the experimental groups (Fig. 4C and 4D). Thus, the increase in vascular density observed following co-exposure to 1000 mGy and HFD was not accompanied by a reduction in pericyte coverage. This finding suggests that the newly observed vessels remained structurally mature and retained pericyte coverage comparable to that of control animals, potentially contributing to the preservation of blood-brain barrier integrity. To investigate the mechanisms underlying the increased vascular density, we next assessed the expression of angiogenesis-related genes, including *Vegf*, *Vegfr1*, *Vegfr2*, and *Angpt2*.

No significant difference in the expression of these angiogenic factors was detected between groups (Fig. 4E). These results suggest that active angiogenic signaling was no longer ongoing at the time of analysis, 6 months after exposure, and may reflect the persistence of vascular changes induced at earlier stages.

We also examined gene expression of angiogenic factors at shorter time points post-irradiation, 15 days and 3 months, to try to explain our increased vascular density. We didn't observe any significant difference in expression across experimental groups, results are presented in supplementary figure S3.

To further assess blood-brain barrier integrity, we examined the expression of genes encoding tight junction proteins. The expression of the tight junction scaffolding protein *Zonula occludens-1* (*Tjp1*) was significantly increased in mice exposed to 1000 mGy alone ($p = 0.045$) and in mice co-exposed to 1000 mGy and HFD ($p = 0.001$). However, expression of genes coding *Claudin1*, *Claudin5* and *Occludin1* did not significantly differ across the groups.

The increase in ZO-1 expression may reflect an adaptive response to reinforce endothelial cell-cell junctions and maintain blood-brain barrier integrity. Combined with the preserved pericyte coverage and the absence of changes in major tight junction proteins, these findings suggest that the observed increase in vascular density is associated with early vascular remodeling rather than overt barrier disruption. Alternatively, the upregulation of *ZO-1* may represent a compensatory mechanism following transient junctional alterations that occurred at earlier time points during the remodeling process.

Exposure to 1000 mGy potentiates the high-fat diet-induced alteration of the plasma metabolomic profile.

Firstly, PLS-DA was performed using Metaboanalyst 6.0 software to evaluate global differences in plasma metabolomic profiles between experimental groups. The resulting PLS-DA score plot showed

only partial separation of the four groups (non-irradiated SD, non-irradiated HFD, irradiated 1000 mGy SD, and irradiated 1000 mGy HFD), indicating ambiguous metabolomic differences. (Fig. 5A)

Component 1 and Component 2 accounted for a total variance of 24.1% in the samples. Inspection of the two-dimensional (2D) score plot (Fig. 5Aa), revealed the significant contribution from Component 1 (16.7%), suggesting a dominant trend in metabolites primarily separating mice according to diet, with a clear distinction between HFD- and SD-fed animals regardless of irradiation status.

In contrast, Component 2 accounted for 7.4% of the variance, suggesting a weaker contribution of irradiation to group segregation, and thus a weaker effect of irradiation on the metabolomic profile across the four groups. Nevertheless, permutation testing confirmed that the overall group classification was statistically significant ($p = 0.003$), supporting the existence of distinct metabolomic signatures across experimental conditions.

The contribution of individual metabolites to group discrimination was assessed using complementary multivariate and univariate approaches. Firstly, metabolites with a Variable Importance in Projection (VIP) score > 1 on Component 2 were selected from the PLS-DA model, resulting in a total of 96 discriminatory metabolites (Fig. 5Ab) Secondly, volcano plot analyses were performed using a significance threshold of FDR p-value < 0.05, and a Fold Change > 1.5 or < 0.66 in metabolite expression in each group compared to the control non-irradiated SD.

Compared with the non-irradiated SD control group, 13 metabolites were significantly up-regulated and 20 down-regulated in non-irradiated HFD-fed mice (Fig. 5Ba). In irradiated SD-fed mice, 13 metabolites were upregulated and 7 were downregulated (Fig. 5Bb). In contrast, the irradiated HFD group exhibited the largest metabolic alterations, with 38 upregulated and 21 downregulated metabolites (Fig. 5Bc). These results indicate that HFD is the primary driver of plasma metabolic changes, whereas irradiation alone induces more limited alterations. Notably, co-exposure to a HFD and 1000 mGy resulted in substantially greater metabolic dysregulation than either stressor alone, suggesting that irradiation potentiates the metabolic disturbances induced by HFD.

To further investigate the specific contribution of irradiation to this metabolic response, pathway enrichment analyses were performed using metabolites selected according the following (2) criteria:(i) a VIP score > 1 on Component 2 and (ii) significant dysregulation in volcano plot analyses following 1000 mGy exposure, regardless of diet, relative to non-irradiated SD controls.To further focus on the metabolites influenced by irradiation, we excluded the 14 metabolites that were also modified by HFD in the absence of irradiation, assuming that they were primarily driven by the diet. This stringent selection strategy reduced reliance on the VIP scores alone, which does not provide p-value information on statistical significance and may be influenced by PLS-DA model susceptible to overfitting [11]. Furthermore, it allows the identification of metabolites deregulated only by 1000 mGy irradiation while minimizing the influence the confounding impact of HFD-induced metabolic changes. As illustrated in the Venn diagram (Fig. 5C), a total of 29 significantly different metabolites meeting these two conditions were identified. The SMPDB pathway analysis (Fig. 5D) on those 29 metabolites shows that the

significantly enriched pathways are related to purine metabolism and the malate-aspartate shuttle. This suggests that exposure to 1000 mGy affects metabolic pathways involved in energy metabolism and nucleotide turnover. Taken together, these findings indicate that while diet represents the main determinant of plasma metabolomic variation, exposure to 1000 mGy amplifies HFD-induced metabolic disturbances and is associated with specific alterations in purine metabolism and the malate–aspartate shuttle.

Discussion

The aim of this study was to determine whether exposure to IR interacts with metabolic stress induced by a HFD to produce cerebrovascular alterations distinct from those induced by either stressor alone. Using a murine model of diet-induced obesity, we investigate long term vascular oxidative, inflammatory, and metabolic responses in the hippocampus 6 months after acute gamma irradiation. Overall, our findings demonstrate that exposure to 1000 mGy, but not 300 mGy, modifies the response to HFD and promotes a phenotype characterized by low-grade neuroinflammation, endothelial activation, vascular remodeling, and systemic metabolic alterations, without evidence of overt endothelial dysfunction or oxidative stress [12].

A key finding of this study is the differential response observed between 300 mGy and 1000 mGy. Exposure to 300 mGy produced minimal long-term effects and was associated with reduced expression of *NFkb1* and *NFkb2*, suggesting a possible attenuation of inflammatory signaling. Similar non-linear responses have previously been reported after low-dose irradiation, where doses around 200 mGy reduced the expression of inflammatory mediators in ApoE-deficient mice [13, 14].

In contrast, exposure to 1000 mGy induced persistent molecular alterations, including decreased *Il6* expression and increased *Il11* and *Zo-1* expression. However, these changes were not accompanied by evidence of oxidative stress, endothelial dysfunction, or marked tissue damage, suggesting the activation of compensatory regulatory processes that may contribute to the maintenance of tissue homeostasis over the long term.

In the present study, six month of HFD alone was insufficient to induce significant oxidative stress, inflammation, alteration of endothelial function, or vascular remodeling. This observation is consistent with the evidence indicating that the vascular consequences of obesity strongly depend on mouse strain, diet composition, and duration of exposure [15]. More severe dietary models such as Western diets enriched in both fat and sucrose, have previously been shown to induce endothelial dysfunction, chronic neuroinflammation, oxidative stress, mitochondrial dysfunction, and microglial activation. Thus, our model appears to represent a moderate metabolic challenge that, by itself, was not sufficient to induce detectable cerebrovascular alterations.

The most pronounced effects were observed following co-exposure to 1000 mGy and HFD. Under these conditions, we detected evidence of low-grade neuroinflammation in the hippocampus, a brain region known to be particularly vulnerable to both metabolic and vascular insults. Although microglial density

remained unchanged, microglia morphology indicated an increase in early activated cells. This observation was accompanied by increased expression of *Ccl2*, *Ccl3*, and *Ccl5* chemokines involved in immune cell recruitment and commonly associated with activated microglia [16]. Increased LYVE-1 immunostaining, further suggests recruitment or expansion of perivascular macrophages, supporting the presence of a localized neuroimmune response [17, 18].

The inflammatory profile observed after co-exposure was complex and could not be fully described using the classical M1/M2 polarization framework. Indeed, recent studies have demonstrated substantial heterogeneity among microglial populations, with multiple activation states coexisting in physiological and pathological conditions [19, 20].

While increased expression of *Nfkb1*, *Nfkb2*, and several chemokines supports activation of inflammatory pathways, the concurrent downregulation of *Il6* and upregulation of *Il-11* suggest activation of compensatory regulatory mechanisms. Together, these findings indicate a state of controlled neuroinflammation rather than a classical pro-inflammatory response.

Endothelial activation appeared to accompany this inflammatory state. Increased *Icam1* expression in the 1000 mGy + HFD group indicates ongoing long-term endothelial activation, compatible with enhanced leukocyte-endothelium interactions and inflammatory signaling. A study of local irradiation of the rat's brain at high doses (20Gy) showed that ICAM-1 was increased in the pial vasculature 48 h post-irradiation but returned to baseline by 7 days [21]. However, endothelial activation after low-dose irradiation remains debated, as results are controversial and inconsistent. Cervelli et al. (2014) showed that X-ray fractionated irradiation at a cumulative dose of 500 mGy led to an increase in the ICAM-1 expression in vitro [22].

While the impact of high doses of IR on endothelial dysfunction is well established, leading to increased oxidative stress [23, 24], inflammation [25, 26], diminished NO-dependent vasodilation [27], impaired hemostasis [28], and weakened vascular integrity [29], all of which promote cardiovascular disease [30, 31].

Nevertheless, no evidence of overt endothelial dysfunction was detected in our study. Expression of *eNOS*, the state of its activating phosphorylation at ser1177, and markers of oxidative stress remained unchanged across groups. These findings suggest that endothelial activation occurred in the absence of measurable impairment of endothelial nitric oxide signaling or redox homeostasis. This distinction is important, as endothelial activation represents a physiological response to tissue stress and does not necessarily progress to endothelial dysfunction.[32] We observed several signs of a regeneration of endothelial network and barrier function. Hippocampal vascular architecture was altered following co-exposure to 1000 mGy and HFD. We observed an increase in the surface occupied by CD31-positive non-muscular vessels, indicating increased vascular density. This change was not associated with reduced pericyte coverage, suggesting that the vascular network remained structurally mature. Furthermore, expression of the tight-junction protein *ZO-1* increased, whereas other blood-brain barrier markers remained unchanged.

Taken together, these observations support the hypothesis of vascular remodeling rather than vascular degeneration or blood-brain barrier disruption. Although we did not detect persistent changes in canonical angiogenic markers such as *Vegf* or its receptors, the angiogenic phase may have occurred prior to the 6-month post-irradiation endpoint of this study.

Our results are consistent with studies showing that HFD alone had little effect on the density of brain vasculature [33]. Capillary rarefaction may occur at longer term, as suggested by Chantler et al. study, that demonstrated capillary rarefaction worsening with time [34]. Our results show that exposure to 1000 mGy, in combination with HFD feeding, was associated with an increased vascular surface.

Furthermore, there was a dose-dependent effect, as we did not observe any change after irradiation at 300 mGy regardless of the diet. In previous studies, whole-brain radiation therapy using 4.5 Gy administered to mice twice weekly for 4 weeks resulted in capillary rarefaction in subregions of the hippocampus [35]. This rarefaction was reversible with systemic hypoxia, which completely restored cerebrovascular density. Additional evidence of reversability of the effects of irradiation in the brain comes from a study where the authors used cranial irradiation with low doses (put the dose value) and demonstrated reversible alteration of the blood-brain barrier [36]. In the moderate dose range, repeated irradiation with 300 mGy for 4 days increased capillary density 45 days post-exposure in a hindlimb ischemia model, with up-regulation of pro-angiogenic factors and their receptors in endothelial cells [37]. Exposure to gamma rays is known to promote angiogenesis and increase metastasis by increasing the expression of VEGF, IL-6, and HIF-1α in the irradiated tissue [38].

The immunostaining ratio of PDGFRβ/CD31 surfaces remained unchanged across exposure groups in our study, suggesting that the increase in vascular density was accompanied by increased pericyte coverage. This indicates that not only was the density of the vascularure increased, but the vascular bed was mature.

Given the observed vascular and inflammatory alterations, and the known effects of both irradiation and obesity on systemic metabolism, we next performed an untargeted metabolomic analysis to determine whether these exposures were associated with long-term metabolic perturbations.

Metabolomic analysis further supported an interaction between irradiation and metabolic stress. While HFD emerged as the main driver of plasma metabolomic alterations, irradiation alone induced more limited changes. Notably, the combination of HFD and 1000 mGy resulted in the highest number of dysregulated metabolites, suggesting that irradiation may exacerbate obesity-associated metabolic disturbances. To better characterize radiation-specific effects, we identified 29 metabolites that were specific to irradiation. Pathway enrichment analysis of these metabolites revealed significant modulation of purine metabolism and the malate-aspartate shuttle. Among the metabolites contributing to the enrichment of the purine metabolism pathway were xanthine, hypoxanthine, and uric acid. These metabolites have previously been proposed as biomarkers of radiation exposure, following the findings of their increased circulating levels in irradiated mice and non-human primates. [39, 40].

In contrast, we observed decreased levels of these metabolites, suggesting activation of the purine salvage pathway. Although this hypothesis requires further investigation, the observed changes may reflect a compensatory metabolic response to cellular stress induced by irradiation. Supporting this possibility, Fujiwara et al. (2022) showed that hypoxanthine supplementation reduced apoptosis and DNA strand breaks in irradiated human umbilical vein endothelial cells through activation of the purine salvage pathway [44]. Differences between our findings and those reported by Fujiwara et al. may be related to the distinct experimental settings, including the use of an in vivo model, the prolonged post-irradiation interval examined here (6 months), and potential differences in radiation dose and exposure conditions.

Beyond its role in the response to DNA damage, the decompensation of the purine salvage pathway has also been associated with increased susceptibility to neurodegenerative processes in the hippocampus [41]. Furthermore, purine metabolism is a key mediator of DNA repair and radioresistance in glioblastoma [42].

Previous studies in non-human primates have reported increased circulating glutamate and other tricarboxylic acid (TCA) cycle intermediates following irradiation, suggesting that alterations in central carbon metabolism may represent a component of the systemic biological response to radiation exposure [47].

. In addition, glutamate can be utilized by endothelial cells for aspartate synthesis which promotes mTORC1 activation, enhancing VEGFR2 translation, and supporting both developmental and pathological angiogenesis [43]. Taken together, these finding suggest that irradiation-induced alterations in purine metabolism and the malate-aspartate shuttle may contribute to systemic adaptive responses involved in DNA repair, cellular survival, and vascular remodeling. Such mechanisms could participate in the neurovascular adaptations observed in the hippocampus of irradiated animals in our study.

In conclusion, our findings suggest that acute exposure to 1000 mGy does not, by itself, induce major cerebrovascular dysfunction but alters the biological response to metabolic stress induced by a 6-month high-fat diet. Six months after irradiation, this state is characterized by low-grade neuroinflammation, endothelial activation, vascular remodeling, and systemic metabolic alterations, while overall vascular integrity remains preserved. Together, these findings indicate that prior irradiation can shape the long-term response to metabolic stress and highlight the importance of considering metabolic challenges when evaluating the biological consequences of ionizing radiation on the cerebrovascular system.

Materials and Methods

Animals

All experiments and procedure were conducted in accordance with the with the European Community guiding principles in the welfare and use of animals (2010/63/UE) and the French decree no. 2013–118 on the protection of animals used for scientific purposes. The protocol was approved by the local

registered ASNR Ethic Committee on Animal Experimentation and by the French Ministry of Higher Education and Research (n° APAFIS #43679-2023053017056324 v3). Male C57BL/6 J mice, aged 7 weeks, were obtained from Janvier Lab (France). The mice were housed in standard laboratory conditions with a 12h light/dark cycle, controlled temperature (22°C ± 2°C), and humidity (55% ± 10%), and ad libitum access to food and water.

Diet

For all experiments, mice were randomly divided into two groups, fed either a standard diet (SD) based on AIN 93M, providing 10.7% of total caloric intake from fat, 13.6% from protein, and 75.6% from carbohydrates (SAFE® U8978 Version 55, SAFE, France), or a high-fat diet (HFD), providing 45.9% of total caloric intake from fat, 17.3% from protein, and 36.8% from carbohydrates (SAFE® U8954 Version 204, SAFE, France).

Irradiation

Upon arrival, the animals acclimated to their new environment and diet for 2 weeks, after which they underwent acute external whole-body gamma irradiation. All irradiations were performed at the CEA (French Alternative Energies and Atomic Energy Commission) with the GSR D1® from GSM, an irradiator using 3 sources of Cesium-137, at a dose-rate of 112 $mGy.min^{-1}$. Mice were randomly divided into three groups, receiving respectively 0 mGy (for the non-irradiated control), 300 mGy, and 1000 mGy of gamma ionizing radiation, respectively.

Euthanasia and tissue collection

The 6-months post-exposure time point was selected to assess the long-term effect of co-exposure to a high-fat diet and acute irradiation. Mice were terminally anesthetized by injection of ketamine (100 $mg.kg^{-1}$)/xylazine (75 $mg.kg^{-1}$) after injection with Buprenorphine (0.05 $mg.kg^{-1}$) and exposure to a mixture of 5% isoflurane and 95% air to reach unconsciousness.

For the histological assay, before terminal anesthesia, mice were perfused with a 4% paraformaldehyde solution (VWR Chemicals). Whole brains were collected and placed in 30% sucrose solution at 4°C overnight. Brains were embedded in Tissue-Tek O.C.T Compound (Sakura OCT 4583). Brain hippocampus sections of 20µm (-0.94 mm to -2.54mm, bregma) were sliced on SuperFrost Plus™ slides (Thermo Scientific™) using a cryostat (NX50, Epredia) and stored at -80°C until use.

For biochemical and molecular biology assays, after terminal anesthesia, by cervical dislocation, the brains were extracted, and the two hemispheres were dissected. The tissues were flash-frozen in liquid nitrogen and stored at -80°C until use, with one hemisphere used for mRNA extraction and the other for protein extraction.

Blood was collected under deep anesthesia by cardiac puncture with heparinized syringe, and plasma was collected after centrifugation at 1000g for 10 minutes. Samples were stored at -80°C until use.

Immunochemistry

Slides were rehydrated in PBS 1X and permeabilized for 30 minutes with 0.1% Triton (X100-100ML, Sigma-Aldrich) in PBS. Slides were blocked for 30 min at room temperature with a protein block solution (E17-100, Zytomics). Primary antibodies prepared in PBS-Triton 0.1% were incubated overnight at 4°C. For microglia identification, an anti-goat Iba1 primary antibody (ab5076, Abcam) was used at a 1/200 dilution. The perivascular macrophages marker LYVE-1, a rabbit anti-LYVE-1 primary antibody (PA1-16635, Invitrogen) was used at a 1/500 dilution. [17] Endothelial cells in blood vessel capillaries were identified using, a rat ant-CD31 primary antibody (553370, BD Pharmigen) at a 1:500 dilution. For pericytes identification, a rabbit anti-PDGFRβ primary antibody (ab32570, Abcam) was used at a 1:200 dilution. The next day, the slides were washed 4 times for 5 minutes with PBS-Triton 0.05%, and incubated with relevant secondary antibodies (1:1000 in PBS-Triton 0.1%) for 2 hours at room temperature. The anti-Iba1 primary antibody was revealed with a Donkey anti-Goat secondary antibody (A32814, Invitrogen), and the anti-Lyve-1 primary antibody was revealed with a Donkey anti-Rabbit secondary antibody (A21207, Invitrogen). The anti-CD31 primary antibody was revealed with a Goat anti-Rat secondary antibody (A11077, Invitrogen), the anti-PDGFRβ primary antibody was revealed with a Goat anti-Rabbit secondary antibody (A11034, Invitrogen).

The slides were then washed 4 times for 5 minutes with PBS-Triton 0.05%, and once for 5 minutes with PBS. Slides were mounted with Vectashield Mounting solution with DAPI (Vector), then scanned using a Nanozoomer S60 (Hamamatsu). The slides were quantified using the QuPath software (v.0.6.0)[44]. Microglial activation was determined semi-quantitatively as previous described by Taetzsch et al. (2015) [45]. Briefly, each slide was examined independently and in a blinded manner by two individuals to establish a standard and assigned score between 0 and 3.

Dihydroéthidium (DHE) staining

For detection of superoxide anion, Dihydroéthidium ThermoFischer) was dissolved in dimethylsulfoxideand used according to the manufacturer's protocol. After 3 washes in PBS, the solution was added to the slides and incubated for 30 minutes at 37°C. The slides were then washed 3 times in PBS, mounted with Vectashield Mounting solution with DAPI (Vector), and scanned using a Nanozoomer S60 (Hamamatsu) and appropriate filters for excitation/emission 302 nm and, 518/605 nm respectively.

RNA extraction and RT-qPCR

The hippocampus was dissected from the frozen half brain in cold PBS in a petri dish on ice and RNA extraction was performed using a QIAzol/chloroform-based protocol. Hippocampus were directly put in 500µL of QIAzol lysis reagent (Qiagen) in lysing matrix D tubes (MP biomedicals) and homogenized by a Precellys® 24 (Bertin Technologies) with a single 20-second cycle at 5500 rpm. The lysate was

centrifuged at 12000 g for 1 minute at 4°C, and transferred to an RNase-free tube. RNA extraction was performed using a standard QIAzol/chloroform-based protocol.

Briefly, 100 µL chloroform was added to the lysate. Sample were vortexed for 30 s, incubated for 3 min at room temperature, centrifuged at 12000 g for 15 min at 4°C. The upper aqueous phase was carefully collected, and RNA was precipitated by adding 300 µL of isopropanol, followed by gentle mixing by inversion. Samples were incubated at room temperature for 10 min and centrifuged at 12000 *g* for 15 min at 4°C. RNA pellets were washed with 75% ethanol and centrifuged at 8000g for 5 min at 4°C. After removal of the supernatant, the pellets were air-dried, resuspended in 40 µL of RNAse-free water. RNA concentration was measured using a NanoDrop ND-1000 spectrophotometer (ThermoFischer), and RNA quality was assessed using a 2100 Bioanalyzer with a RNA 6000 Nano Kit (Agilent).

Reverse transcription was performed with the high-capacity cDNA Reverse Transcription Kit from Applied Biosystems (Life Technologies) and a thermocycler (SimpliAmp, Applied Biosystem) following the kit's temperature cycle recommendations. RNAsa-free water was added to reach a cDNA concentration of 50ng.µL^{-1}, and cDNA were stored at -20°C until use.

qPCR was carried out using a QuantStudio 12K Flex Real-Time PCR System (ThermoFisher) in MicroAmp® Optical 384-well plates (Applied Biosystems) in duplicate. For each reaction, 4µL cDNA diluted at 1:40, 6µL SYBR green and respective ready-to-use PCR primers for mouse, synthesized by Qiagen (Quantitect Primer Assay, Qiagen), were distributed by an EpMotion 5073 (Eppendorf). Primers are detailed in table 1 in supplementary method.

Samples were assayed in duplicate and normalized with two house-keeping genes: Gapdh and Hprt1. GAPDH et HPRT.

Protein extraction and Western Blot

Hippocampus were placed in lysing matrix D tubes (MP biomedicals) containing 150µL of RIPA lysis buffer (ThermiFischer®) with protease inhibitors (cOmplete Tablets EASYpack, Roche). Tissues were homogenized by a Precellys® 24 (Bertin Technologies) with a single 20-second cycle at 5500 rpm. After a short centrifugation for 1 min at 1500g, 4°C, samples were stored at -80°C until use.

Protein concentration was assessed using a Pierce™ Rapid Gold BCA Protein Assay Kit (Thermo Fisher Scientific®, USA), absorbance was read at 480 nm on an Infinite M200 pro (TECAN®).

SDS-PAGE was carried out using 40 µg proteins after samples denaturation in Laemmli 4× buffer (Bio-Rad) and Reducing Agent 20× (Bio-Rad). Samples were denatured at 37°C for 30 minutes and then transferred in 15-well 10% acrylamide gels (Mini-PROTEAN TGX Stain-Free precast gels, Bio-Rad®). Migration was carried out for 10 minutes at 70 Volts, followed by 1 hour and 20 minutes at 110 Volts on a Mini-PRETEAN® Tetra cell (Bio-Rad®) with a water and TGS 10X buffer (Bio-Rad®). Proteins were then transferred onto a membrane (Trans Blot Turbo™ Mini-PVDF Transfer Packs, Bio-Rad®) using a Trans-

Blot Turbo (BioRad®) for 7min at 2.5A and 25 V. Stain-free detection was done on GelDoc Go Imaging System (Bio-Rad®), to detect total protein level in each sample.

Primary antibodies dilutions were prepared at 1:1000 dilution in 2.5% milk in PBS -Tween and incubated overnight at 4°C under gentle shaking. (ENOS, ref: ab199956, Abcam ; p-ENOS ser 1177, ref:PA5-97371, Invitrogen). The membranes were then washed in PBS-Tween 0.1% for 3 minutes 5 times. The respective secondary HRP-conjugated anti-rabbit antibody (HAF008, Novus Biologicals) was diluted to 1:5000 in 2.5% milk in PBS-Tween 0.1% and added, then incubated for 2 h. After 5 3-minute washes in PBS-Tween, membranes were revealed, using chemiluminescence reagents according to the manufacturer's protocol (Supersignal West Pico Plus chemiluminescence substrate PIER34578, Thermo Fischer Scientific) and an ImageQuant™800 (Cytiva) imager. Acquired images were quantified using the ImageQuant™ software (ImageQuant TL 10.0.261, Cytiva). Stain-free total protein signal was used for normalization.

Metabolomic

For metabolomic analysis, 100µL of plasma was sent to the CriBioM platform at the Centre Cardiovasculaire et Nutrition (C2VN, Marseille, France). Sample preparation, spectrometry analysis, and data processing are described in detail in supplementary material.. Data were analyzed and discriminant variables were interpreted using Metaboanalyst 6.030. Small Molecule Pathway Database (https://smpdb.ca) was used with the specific MetaboAnalyst module (https// www.metaboanalyst.ca) to analyze pathway enrichment and discriminate data according to their involvement in metabolic and biological functions.

Statistical analysis

The statistical analyses were performed using Prism 8.4.2 (GraphPad Software). Normality was assessed using Shapiro-Wilk test. If the null hypothesis was accepted, data were considered normally distributed, and were analyzed using One-way ANOVA, followed by multiple comparisons using Tukey's HSD post-hoc test. If the null hypothesis was rejected, the nonparametric Kruskal-Wallis test was used with Dunn's post hoc test for multiple comparisons. All data presented in the figures are reported as means ± standard deviation (StdDev); the significance level was set at $P < 0.05$. P-values are reported in the text, with significance levels indicated as follows: * $P < 0.05$, ** $P < 0.01$, *** $P < 0.001$.

Data availability statement

The data that support the findings of this study are available from the corresponding author, upon reasonable request.

Declarations

Acknowledgements

This work was supported by grants from Electricité de France (EDF) and by the Autorité de Sûreté Nucléaire et de Radioprotection (ASNR).

Author contribution

Conceptualization: Teni G. Ebrahimian

Data curation: Léa Ould Boukhitine, Chloé Brizais, Florence Bachelot, Yasmine Ebid, Imane Lahyouli

Formal analysis: Léa Ould Boukhitine, Imène Garali, Teni G. Ebrahimian, Florence Bachelot, Yasmine Ebid

Funding acquisition: Teni G. Ebrahimian

Investigation : Léa Ould Boukhitine, Chloé Brizais, Florence Bachelot, Chrystelle Ibanez, Yasmine Ebid, Imane Lahyouli, Mouna Chajadine

Methodology: Léa Ould Boukhitine, Teni G. Ebrahimian, Chloé Brizais, Chrystelle Ibanez, Christelle Durand, Florence Bachelot,Stéphane Grison

Supervision: Teni G. Ebrahimian, Boris Manoury

Validation: Léa Ould Boukhitine, Florence Bachelot, Teni G. Ebrahimian, Boris Manoury

Visualization: Léa Ould Boukhitine

Writing—original draft: Léa Ould Boukhitine

Writing—review & editing: Teni G. Ebrahimian, Boris Manoury, Dmitry Klokov

References

1. Ivanov, V., Ilyin, L., Gorski, A., Tukov, A. & Naumenko, R. Radiation and epidemiological analysis for solid cancer incidence among nuclear workers who participated in recovery operations following the accident at the Chernobyl NPP. *J. Radiat. Res. (Tokyo)*. **45**, 41–44 (2004).
2. Rajaraman, P. et al. Factors governing individual response to ionizing radiation and risk of diseases of the circulatory system: human epidemiological studies. *Int. J. Radiat. Biol.* 1–13. 10.1080/09553002.2025.2561808 (2025).
3. Stewart, F. A. et al. Ionizing radiation accelerates the development of atherosclerotic lesions in ApoE-/- mice and predisposes to an inflammatory plaque phenotype prone to hemorrhage. *Am. J. Pathol.* **168**, 649–658 (2006).
4. Seemann, I. et al. Irradiation induced modest changes in murine cardiac function despite progressive structural damage to the myocardium and microvasculature. *Radiother Oncol.* **103**, 143–150 (2012).
5. Zimmerman, B., Kundu, P., Rooney, W. D. & Raber, J. The Effect of High Fat Diet on Cerebrovascular Health and Pathology: A Species Comparative Review. *Molecules* **26**, 3406 (2021).

6. Kanoski, S. E., Zhang, Y., Zheng, W. & Davidson, T. L. The Effects of a High-Energy Diet on Hippocampal Function and Blood-Brain Barrier Integrity in the Rat. *J. Alzheimer's Dis.* **21**, 207–219 (2010).
7. Tribble, D. L., Barcellos-Hoff, M. H., Chu, B. M. & Gong, E. L. Ionizing Radiation Accelerates Aortic Lesion Formation in Fat-Fed Mice via SOD-Inhibitable Processes. *Arterioscler. Thromb. Vasc Biol.* **19**, 1387–1392 (1999).
8. Liu, X. et al. Low-dose radiation promotes high-fat diet-induced atherosclerosis by activating cGAS signal pathway. *Biochim. Biophys. Acta Mol. Basis Dis.* **1870**, 167443 (2024).
9. Kantapan, J., Katsube, T. & Wang, B. High-Fat Diet and Altered Radiation Response. *Biology* **14**, 324 (2025).
10. Ju, Z. et al. Low-dose radiation exaggerates HFD-induced metabolic dysfunction by gut microbiota through PA-PYCR1 axis. *Commun. Biol.* **5**, 945 (2022).
11. Ruiz-Perez, D., Guan, H., Madhivanan, P., Mathee, K. & Narasimhan, G. So you think you can PLS-DA? *BMC Bioinform.* **21**, 2 (2020).
12. Cavaliere, G. et al. High-Fat Diet Induces Neuroinflammation and Mitochondrial Impairment in Mice Cerebral Cortex and Synaptic Fraction. *Front. Cell. Neurosci.* **13**, 509 (2019).
13. Rey, N. et al. Exposure to Low to Moderate Doses of Ionizing Radiation Induces A Reduction of Pro-Inflammatory Ly6chigh Monocytes and a U-Curved Response of T Cells in APOE -/- Mice. *Dose-Response Publ Int. Hormesis Soc.* **19**, 15593258211016237 (2021).
14. Rey, N. et al. Low to moderate dose 137Cs (γ) radiation promotes M2 type macrophage skewing and reduces atherosclerotic plaque CD68 + cell content in ApoE(−/−) mice. *Sci. Rep.* **14**, 12450 (2024).
15. Lang, P., Hasselwander, S., Li, H. & Xia, N. Effects of different diets used in diet-induced obesity models on insulin resistance and vascular dysfunction in C57BL/6 mice. *Sci. Rep.* **9**, 19556 (2019).
16. Kremlev, S. G., Roberts, R. L. & Palmer, C. Differential expression of chemokines and chemokine receptors during microglial activation and inhibition. *J. Neuroimmunol.* **149**, 1–9 (2004).
17. Siret, C. et al. Deciphering the heterogeneity of the Lyve1 + perivascular macrophages in the mouse brain. *Nat. Commun.* **13**, 7366 (2022).
18. Zrzavy, T. et al. Dominant role of microglial and macrophage innate immune responses in human ischemic infarcts. *Brain Pathol.* **28**, 791–805 (2018).
19. Ransohoff, R. M. A polarizing question: do M1 and M2 microglia exist? *Nat. Neurosci.* https://doi.org/10.1038/nn.4338 (2016).
20. Hammond, T. R. et al. Single-Cell RNA Sequencing of Microglia throughout the Mouse Lifespan and in the Injured Brain Reveals Complex Cell-State Changes. *Immunity* **50**, 253–271e6 (2019).
21. Yuan, H. et al. Radiation-Induced Up-regulation of Adhesion Molecules in Brain Microvasculature and their Modulation by Dexamethasone. *Radiat. Res.* **163**, 544–551 (2005).
22. Cervelli, T. et al. Effects of single and fractionated low-dose irradiation on vascular endothelial cells. *Atherosclerosis* **235**, 510–518 (2014).

23. Collins-Underwood, J. R., Zhao, W., Sharpe, J. G. & Robbins, M. E. NADPH oxidase mediates radiation-induced oxidative stress in rat brain microvascular endothelial cells. *Free Radic Biol. Med.* **45**, 929–938 (2008).
24. Azzam, E. I., Jay-Gerin, J. P. & Pain, D. Ionizing radiation-induced metabolic oxidative stress and prolonged cell injury. *Cancer Lett.* **327**, 48–60 (2012).
25. Di Maggio, F. M. et al. Portrait of inflammatory response to ionizing radiation treatment. *J. Inflamm. Lond. Engl.* **12**, 14 (2015).
26. Schaue, D. et al. Radiation & Inflammation. *Semin Radiat. Oncol.* **25**, 4–10 (2015).
27. Soloviev, A. I. et al. Mechanisms of endothelial dysfunction after ionized radiation: selective impairment of the nitric oxide component of endothelium-dependent vasodilation. *Br. J. Pharmacol.* **138**, 837–844 (2003).
28. Baselet, B., Sonveaux, P., Baatout, S. & Aerts, A. Pathological effects of ionizing radiation: endothelial activation and dysfunction. *Cell. Mol. Life Sci. CMLS*. **76**, 699–728 (2018).
29. Venkatesulu, B. P. et al. Radiation-Induced Endothelial Vascular Injury: A Review of Possible Mechanisms. *JACC Basic. Transl Sci.* **3**, 563–572 (2018).
30. Darby, S. C. et al. Radiation-related heart disease: current knowledge and future prospects. *Int. J. Radiat. Oncol. Biol. Phys.* **76**, 656–665 (2010).
31. Shimizu, Y. et al. Radiation exposure and circulatory disease risk: Hiroshima and Nagasaki atomic bomb survivor data, 1950–2003. (2010). https://doi.org/10.1136/bmj.b5349 doi:10.1136/bmj.b5349.
32. Palomo, M. et al. Endothelial activation and damage as a common pathological substrate in different pathologies and cell therapy complications. *Front Med* **10**, (2023).
33. Pakarinen, E. et al. High-fat diet feeding induces organ-specific vascular remodeling with distinct temporal dynamics in male mice. *Commun. Biol.* **9**, 888 (2026).
34. Chantler, P. D. et al. Cerebral Cortical Microvascular Rarefaction in Metabolic Syndrome is Dependent on Insulin Resistance and Loss of Nitric Oxide Bioavailability. *Microcirculation* **22**, 435–445 (2015).
35. Warrington, J. P. et al. Cerebral microvascular rarefaction induced by whole brain radiation is reversible by systemic hypoxia in mice. *Am. J. Physiol. Heart Circ. Physiol.* **300**, H736–744 (2011).
36. Sándor, N. et al. Low Dose Cranial Irradiation-Induced Cerebrovascular Damage Is Reversible in Mice. *PLOS ONE*. **9**, e112397 (2014).
37. Ministro, A. et al. Low-dose ionizing radiation induces therapeutic neovascularization in a pre-clinical model of hindlimb ischemia. *Cardiovasc. Res.* **113**, 783–794 (2017).
38. Grabham, P. & Sharma, P. The effects of radiation on angiogenesis. *Vasc Cell.* **5**, 19 (2013).
39. Johnson, C. H. et al. Radiation Metabolomics. 5. Identification of Urinary Biomarkers of Ionizing Radiation Exposure in Nonhuman Primates by Mass Spectrometry-Based Metabolomics. *Radiat. Res.* **178**, 328–340 (2012).

40. Pannkuk, E. L., Laiakis, E. C., Authier, S., Wong, K. & Fornace, A. J. Global Metabolomic Identification of Long-Term Dose-Dependent Urinary Biomarkers in Nonhuman Primates Exposed to Ionizing Radiation. *Radiat. Res.* **184**, 121–133 (2015).
41. Long, X. et al. Comprehensive metabolic profiling across five lifespan stages in murine hippocampus and cortex reveals sex-related variation in age-related cognitive decline. *Commun. Biol.* **9**, 249 (2026).
42. Zhou, W. et al. Purine metabolism regulates DNA repair and therapy resistance in glioblastoma. *Nat. Commun.* **11**, 3811 (2020).
43. Oberkersch, R. E. et al. Aspartate metabolism in endothelial cells activates the mTORC1 pathway to initiate translation during angiogenesis. *Dev. Cell.* **57**, 1241–1256e8 (2022).
44. Bankhead, P. et al. QuPath: Open source software for digital pathology image analysis. *Sci. Rep.* **7**, 16878 (2017).
45. Taetzsch, T. et al. Redox Regulation of NF-κB p50 and M1 Polarization in Microglia. *Glia* **63**, 423–440 (2015).

Table 1

Table 1 is available in the Supplementary Files section.

Figures

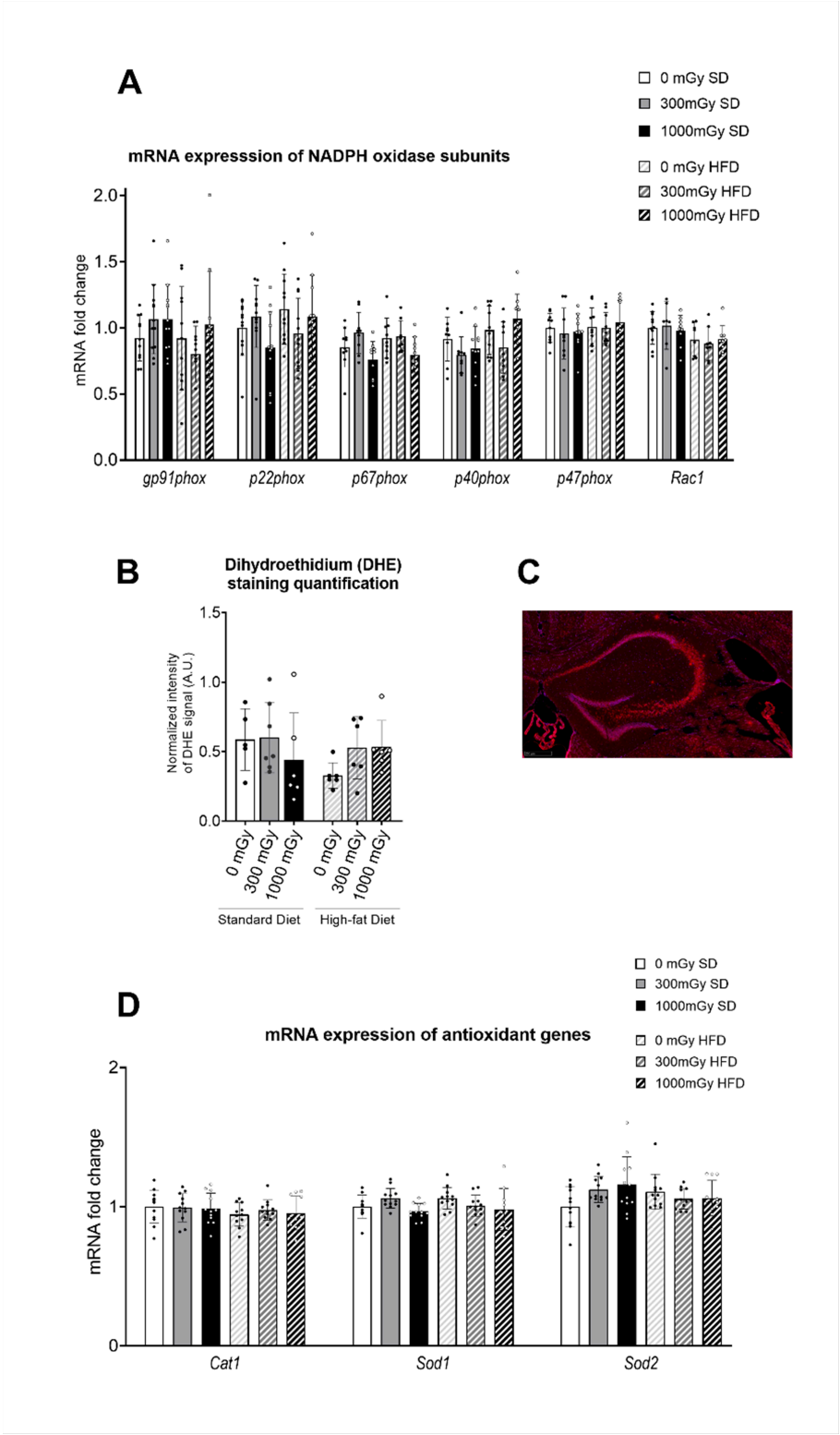


Figure 1

NADPH oxidase and antioxidant-linked gene expression and superoxide anion staining. (**A**) Relative mRNA expression of NADPH oxidase sub-units determined by quantitative RT-PCR and expressed as fold change relative to non-exposed control mice ± SD. *n* = 7-12 per group (**B**) Quantification of superoxide anion by DHE staining intensity ± SD. Arbitrary units (A.U.). *n* = 6 per group. (**C**) Illustration of DHE staining in the hippocampus. (**D**) Relative mRNA expression of *Cat1*, *Sod1*, and *Sod2* determined by

quantitative RT-PCR and expressed as fold change relative to non-exposed control mice ± SD. *n* = 8-12 per group.

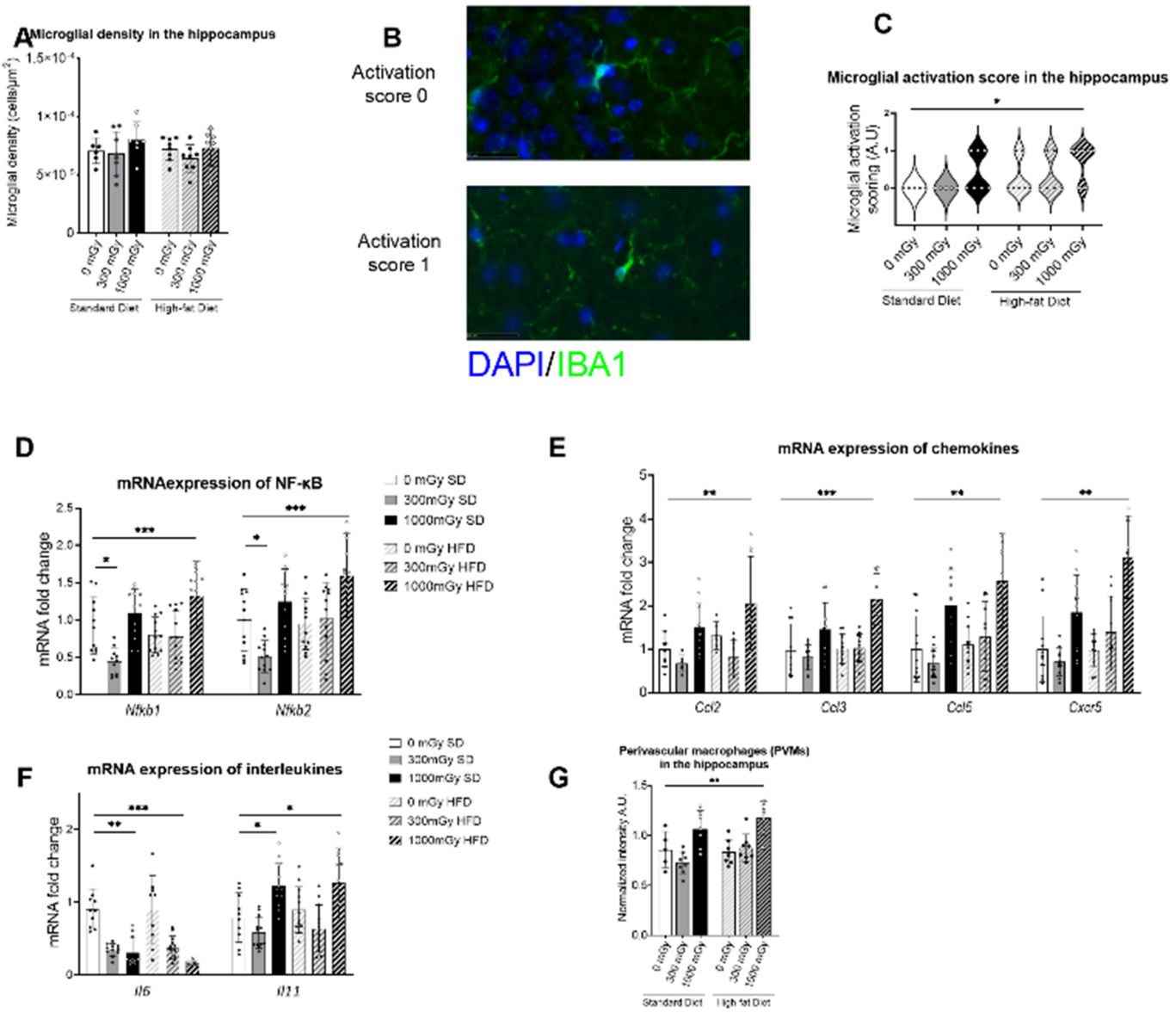


Figure 2

Inflammatory response in the hippocampus. (**A**) Microglial density quantification in the number of marked cells per µm2 ± SD. *n* = 6-8 per group. (**B**) Illustration of microglial cells stained with a Iba1 (green) and DAPI (blue) (**C**) Microglial activation scoring ± SD. Arbitrary units (A.U.). *n* = 6-8 per group. Statistical analysis was performed using Pearson's Chi-squared test. *$p < 0.05$. (**D**) Relative mRNA expression of *Nfkb1*, *Nfkb2*determined by quantitative RT-PCR and expressed as fold change relative to non-exposed control mice ± SD. *n* = 10-12 per group. (**E**) Relative mRNA expression of interleukines (*Il6*, *Il11)* determined by quantitative RT-PCR and expressed as fold change relative to non-exposed control mice ± SD. *n* = 10-12 per group. (**F**) Relative mRNA expression of chemokines and receptors (*Ccl2, Ccl3,*

Ccl5, Cxcr5) determined by quantitative RT-PCR and expressed as fold change relative to non-exposed control mice ± SD. *n* = 10-12 per group. (**G**) Perivascular macrophages quantification by ratio of *Lyve-1* intensity immunostaining on hippocampus surface ± SD. Arbitrary units (A.U.). *n* = 5-8 per group. Results passed normality tests for figures A, D and G and were analyzed using one-way ANOVA followed by Tukey's multiple-comparison test. Results for figures E and F did not pass the normality test and were analyzed using Kruskal–Wallis test followed by Dunn's post hoc test. All groups were compared to each other and significant differences between groups are indicated as follows: *$p < 0.05$; **$p < 0.01$.

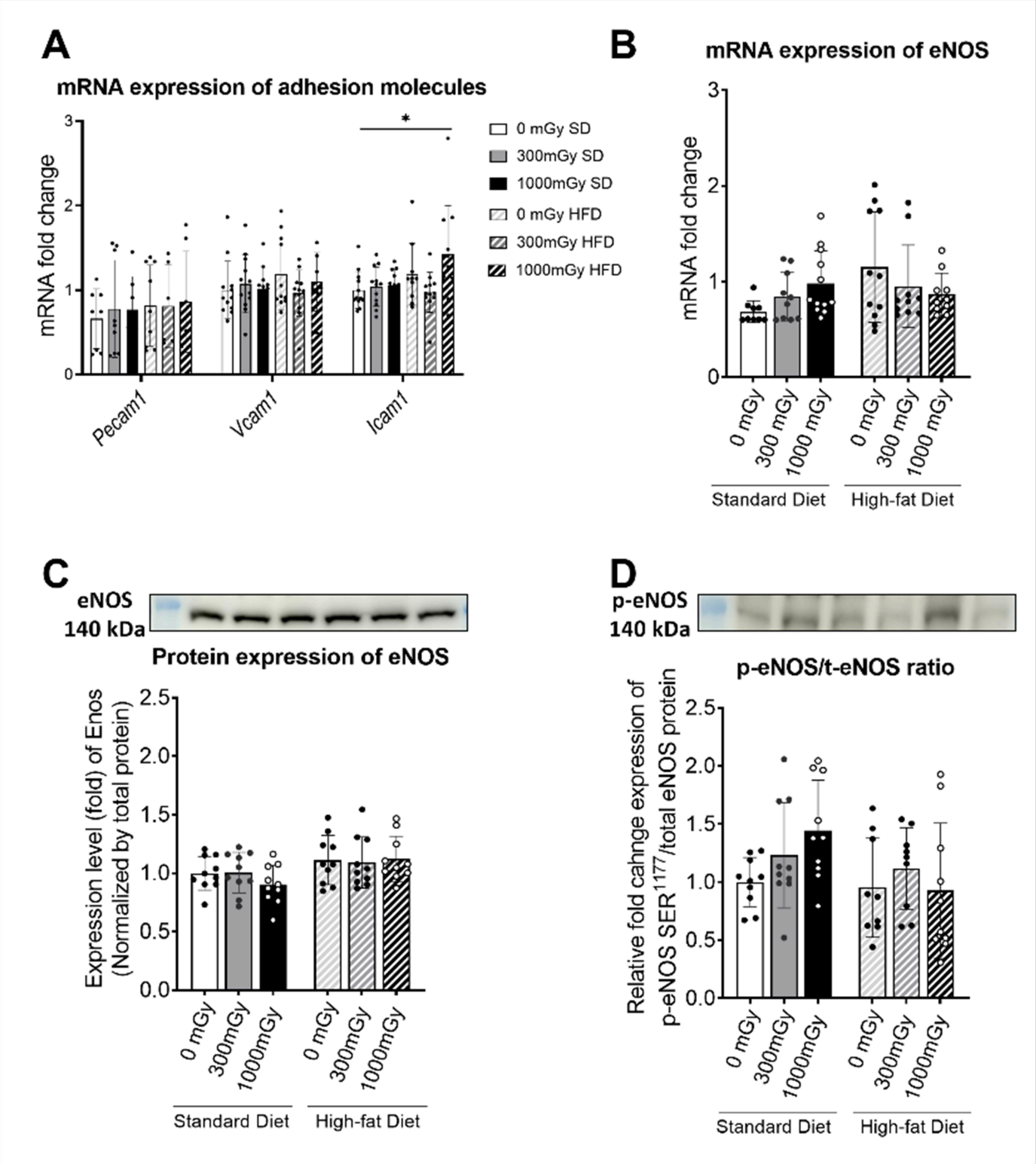


Figure 3

Endothelial dysfunction markers: adhesion molecules and eNOS. (**A**) Relative mRNA expression of adhesion molecules (*Pecam1*, *Vcam1*, *Icam1)* determined by quantitative RT-PCR and expressed as fold change relative to non-exposed control mice ± SD. *n* = 8-12 per group. (**B**) Relative mRNA expression of *eNOS* determined by quantitative RT-PCR and expressed as fold change relative to non-exposed control mice ± SD. *n* = 9-12 per group. (**C**) Western blot analysis of *eNOS* protein expression level expressed as fold change relative to non-exposed control mice ± SD. *n* = 8-10 per group. (**D**) Western blot analysis of *phospho-eNOS* (Ser 1177) expressed as ratio relative to *eNOS*total protein expression level ± SD. *n* = 10 per group. Western blot membranes images were cropped (Figure 3C and D) and original blots are presented in Supplementary Figure S2. Results for figure A did not pass the normality test and were analyzed using Kruskal–Wallis test followed by Dunn's post hoc test. All groups were compared to each other, and significant differences between groups are indicated as follows: $*p < 0.05$.

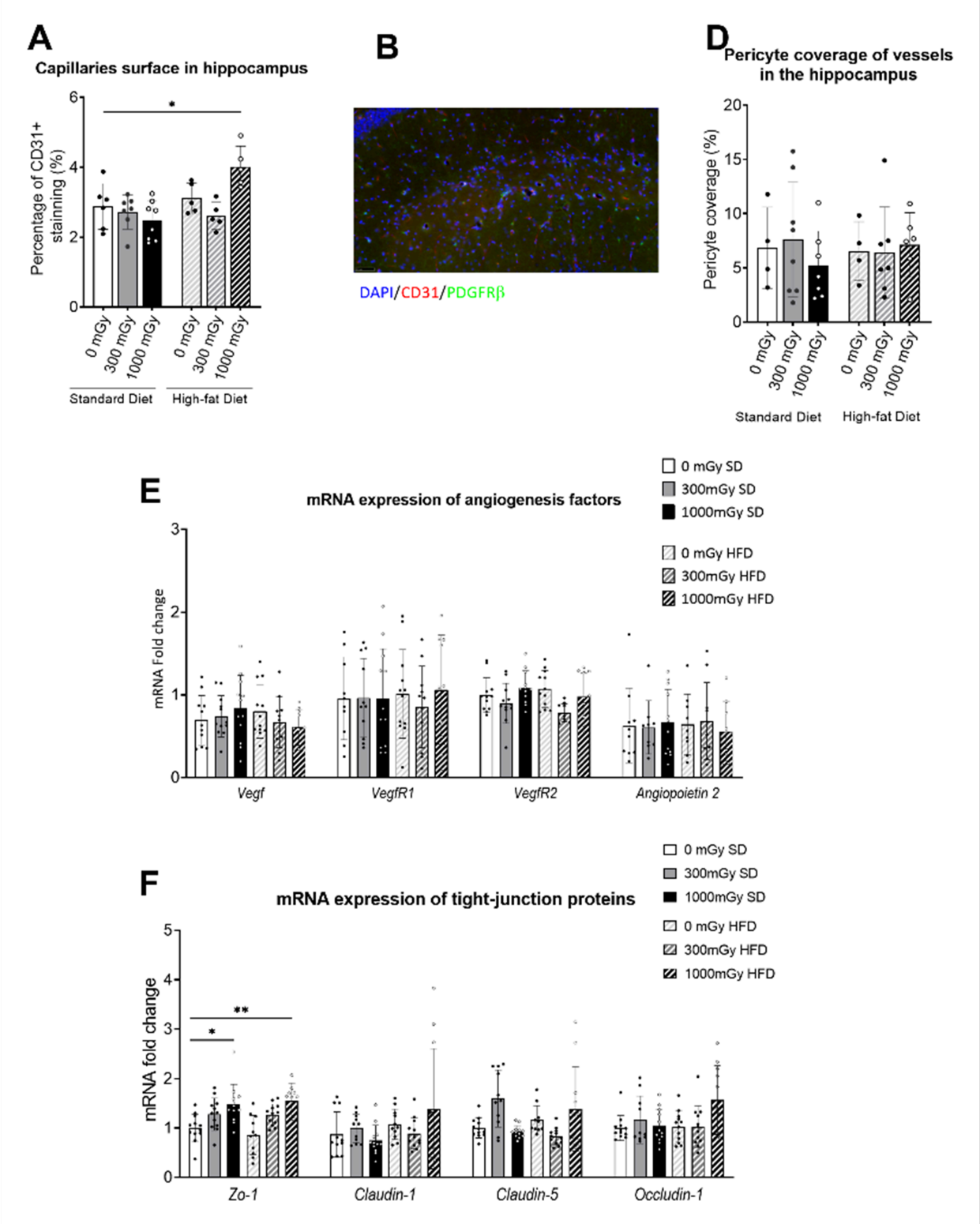


Figure 4

Vascular density in the hippocampus. (**A**) Percentage of capillary surface in the hippocampus quantified by CD31-positive and a-SMA negative surface relative to hippocampus area in percentage ± SD. *n* = 4-8 per group. (**B**) Illustration of endothelial cells stained with CD31 (red) and DAPI (blue). (**C**) Illustration of capillaries: endothelial cells stained with CD31 (red), pericytes stained with PDGFR-b (green), and nuclei stained with DAPI (blue). (**D**) Pericyte coverage of blood vessel quantified by PDGFR-b positive surface

on CD31 positive surface ± SD. *n* = 4-8 per group. (**E**) Relative mRNA expression of angiogenic factors (*Vegfa*, *Vegf-R1*, *Vegf-R2, Angpt2)* determined by quantitative RT-PCR and expressed as fold change relative to non-exposed control mice ± SD. *n* = 9-12 per group. (**E**) Relative mRNA expression of tight-junction proteins (*ZO-1*, *Claudin-1*, *Claudin-5, Occludin-1)* determined by quantitative RT-PCR and expressed as fold change relative to non-exposed control mice ± SD. *n* = 8-12 per group. Results passed normality tests for figures A and D and were analyzed using one-way ANOVA followed by Tukey's multiple-comparison test. Results for figures E and F did not pass the normality test and were analyzed using Kruskal–Wallis test followed by Dunn's post hoc test. All groups were compared to each other and significant differences between groups are indicated as follows: $*p < 0.05$; $**p < 0.01$

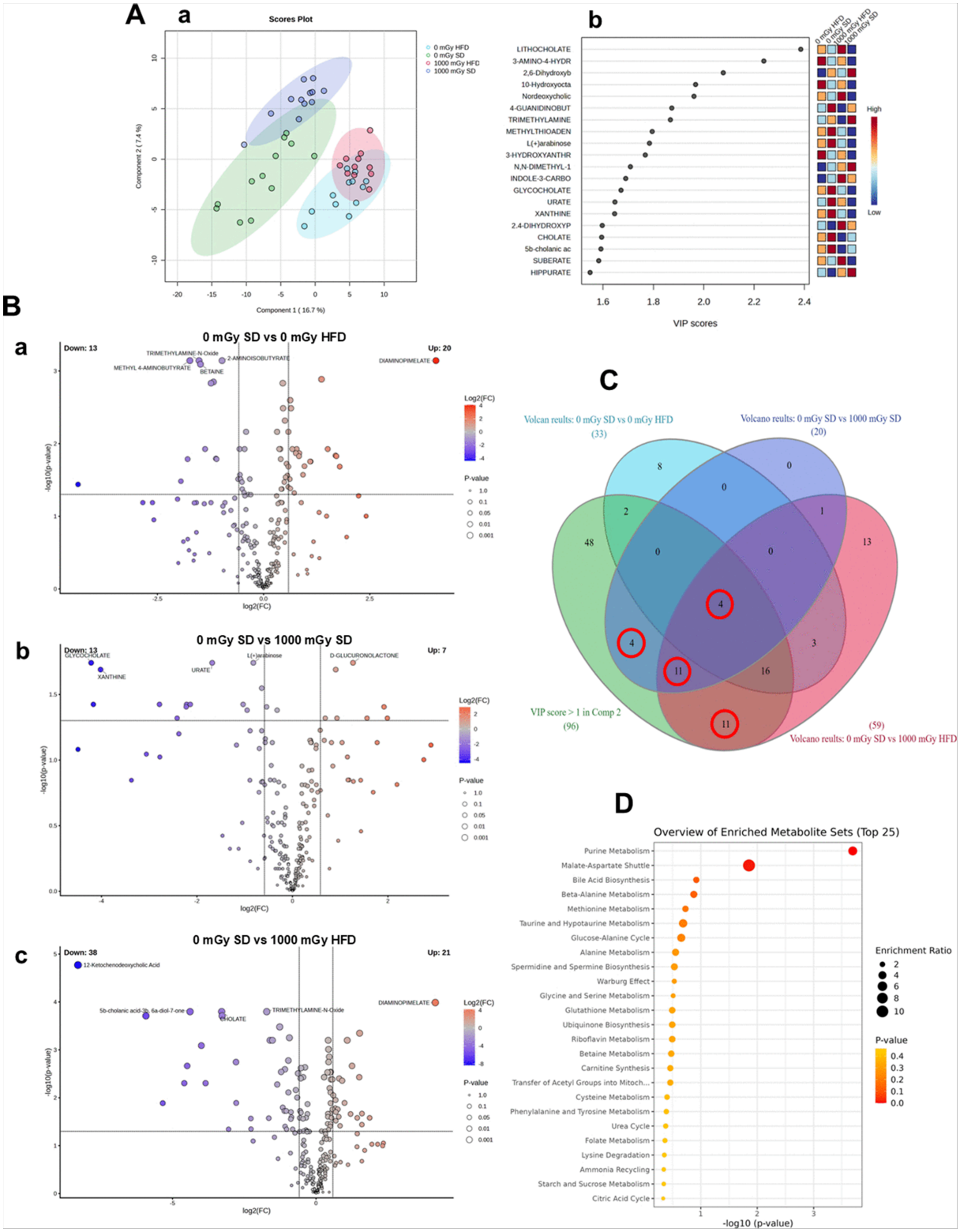


Figure 5

Multivariate analysis of metabolomics data in plasma (**A**) Multivariate analysis of the metabolomics data: comparison between every group, non-irradiated and irradiated at 1000 mGy, fed with a standard or high-fat diet. (**a**) Partial least-squares discriminant analysis (PLS-DA). (**b**) Top 20 metabolite features ranked according to their Variable importance in projection (VIP) scores in component 2 (VIP scores > 1) (**B**) Volcan plot showing relative abundances of metabolites. Significance is defined by a LIMMA t-test p-

value FDR≤ 0.05 and a result of fold change analysis (treated group/control group 0 mGy SD) >1.5 or <0.66. (**a**) Volcano plots showing the relative abundances of metabolites between group exposed to 0 mGy HFD and control group 0 mGy SD. (**b**) Volcano plots showing the relative abundances of metabolites between group exposed to 1000 mGy SD and control group 0 mGy SD. (**c**) Volcano plots showing the relative abundances of metabolites between group exposed to 1000 mGy HFD and control group 0 mGy SD. (**C**) Venn diagram representing the number of significantly differential dysregulated metabolites in each group compared to the control 0 mGy SD detected by the Volcano Plot analysis and PLS-DA VIP score. The metabolites circled in red were used for metabolic pathway enrichment analysis. (**D**) Summary of metabolic pathway enrichment analysis with SMPDB using a set of 29 metabolites found to be significantly dysregulated by irradiation compared to control.

Supplementary Files

This is a list of supplementary files associated with this preprint. Click to download.

- Supplementarymaterial.pdf
- Supplementaryinformationrevised.pdf